Migration of Earth-sized planets in 3D radiative discs

E. Lega,[★] A. Crida,[★] B. Bitsch[★] and A. Morbidelli[★]

Université Nice Sophia Antipolis, CNRS UMR 7293, Observatoire de la Côte d'Azur, Bv. de l'Observatoire, CS 34229, F-06304 Nice cedex 4, France

ABSTRACT

In this paper, we address the migration of small-mass planets in 3D radiative discs. Indeed, migration of small planets is known to be too fast inwards in locally isothermal conditions. However, thermal effects could reverse its direction, potentially saving planets in the inner, optically thick parts of the protoplanetary disc. This effect has been seen for masses larger than 5 Earth masses, but the minimum mass for this to happen has never been probed numerically, although it is of crucial importance for planet formation scenarios. We have extended the hydrodynamical code FARGO to 3D, with thermal diffusion. With this code, we perform simulations of embedded planets down to 2 Earth masses. For a set of discs' parameters for which outward migration has been shown in the range of [5, 35] Earth masses, we find that the transition to inward migration occurs for masses in the range [3, 5] Earth masses. The transition appears to be due to an unexpected phenomenon: the formation of an asymmetric cold and dense finger of gas driven by circulation and libration streamlines. We recover this phenomenon in 2D simulations where we control the cooling effects of the gas through a simple modelling of the energy equation.

Key words: hydrodynamics – methods: numerical – protoplanetary discs – planetary systems.

1 INTRODUCTION

The cores of giant planets and possibly many super-Earths form and migrate within a protoplanetary disc. In a locally isothermal disc, planets with masses $m_p \lesssim 10-15$ Earth masses ($M_\oplus$) are expected to undergo type-I migration towards the central star on a time-scale proportional to $1/m_p$ (Tanaka, Takeuchi & Ward 2002), which can be shorter than the disc's lifetime for $m_p \gtrsim 1 \, M_\oplus$. If this were true, planetary cores should not survive in the disc, in evident contrast with the observation that many planetary systems, including our own, have planets that are not even very close to the star.

Many efforts have been done to solve this puzzling problem. Different mechanisms have been suggested to halt inward migration such as magnetic field effects in turbulent discs (Baruteau et al. 2011; Guilet, Baruteau & Papaloizou 2013, and references therein) or density trap (Masset 2002; Masset et al. 2006a; Morbidelli et al. 2008). But, perhaps the most promising mechanism appears when considering the effect of energy transfer within the disc. Studies have shown that non-isothermal effects can change the direction of the type-I migration (Paardekooper & Mellema 2006; Baruteau & Masset 2008; Kley & Crida 2008; Kley, Bitsch & Klahr 2009; Masset & Casoli 2009, 2010; Paardekooper et al. 2010).

Precisely, the migration in the inner part of a radiative disc can be directed outwards, while it remains directed inwards in the outer

disc. This establishes the existence of a critical radius where migration vanishes, towards which planetary cores migrate from both the inner and the outer part of the disc. Therefore, the zero migration location acts as a planet trap (Lyra, Paardekooper & Mac Low 2010).

The torque exerted by the protoplanetary disc has two main contributions: (i) the so-called Lindblad torque due to the spiral arms launched by the planet in the disc which is not affected by the equation of state (EOS)[1] and (ii) the corotation torque caused by material librating in the horseshoe region. When considering radiative effects, it has been shown that the corotation torque contribution can be positive and possibly dominate over the negative Lindblad torque. In a recent paper, Paardekooper, Baruteau & Kley (2011) have provided a detailed formula for the torque which was calibrated with a 2D hydrodynamical model for low-mass planets (5 $M_\oplus$). However, the corotation effect depends on the disc parameters and on the mass of the planet. Decreasing the planetary mass, the horseshoe U-turn time-scale increases and, if it becomes longer than the radiative diffusion time-scale, the disc behaves similarly to the isothermal case and the positive torque contribution fades.

The aim of this paper is to investigate the total torque acting on low-mass planets kept on fixed orbits and possibly find the critical mass for which the positive contribution of the corotation torque becomes smaller than the Lindblad torque. To this purpose, we

★ E-mail: elena@oca.eu (EL); aurelien.crida@oca.eu (AC); bbitsch@oca.eu (BB); morby@oca.eu (AM)

---

[1] Actually, it scales with $\gamma \Gamma_0$, with Γ_0 given in equation (4).

have extended the FARGO code of Masset (2000a), Masset (2000b) to three dimensions introducing an energy equation to provide a realistic modelling of radiative effects as in Kley et al. (2009). We have validated the three-dimensional version of FARGO (FARGO with Colatitude Added, FARGOCA hereafter) by reproducing some results published in the literature (see Appendix).

We have computed the total torque on planets with mass ranges in the interval [2, 10] Earth masses for a specific set of disc parameters and we found that a transition from positive to negative total torque occurs for a planet with mass between 3 and 5 Earth masses. We remark that for the same disc parameters, Kley et al. (2009) found positive total torque for planetary masses in the range [5, 35] Earth masses. When applying the torque formula provided in Paardekooper et al. (2011) to our disc parameters, we find a transition from outward to inward migration occurring between 2.7 and 3 Earth masses.

Despite the good agreement between model and simulations, it is important to study the mechanism that causes the transition, since in the case of Paardekooper et al. (2011), the results were calibrated with 2D simulations while our work is done with numerical simulations of a full radiative 3D model. For this purpose, we have analysed the torque suffered by the planet from every radial ring of the disc. We have found a new and unexpected feature: a negative contribution to the torque that is not seen for planetary masses larger than $m_p \gtrsim 5\,M_\oplus$. This is due to an overdensity of gas behind the planet location just outside of its orbit.

We have recovered the same effect in 2D simulations where the energy equation has a simple cooling prescription in which the cooling time appears as a parameter. Despite its simplicity, the 2D model allows us to confirm the result and to study its dependence on the gas cooling time-scale.

The paper is organized as follows: the physical modelling is presented in Section 2, in Section 3, total torque calculations on small-mass planets are described. We provide in Section 4 a detailed analysis of the local torque acting on the planets as well as a mechanism for the origin of the negative and positive local contributions to the torque that we observe on small-mass planets. We validate the proposed mechanism in Section 5 using 2D simulations. In Section 6, we explain the origin of the asymmetry between negative and positive torque contributions. Conclusions are provided in Section 7. In the appendix, we provide test calculations on the FARGOCA code.

2 PHYSICAL MODELLING

The protoplanetary disc is treated as a three-dimensional non-self-gravitating gas whose motion is described by the Navier–Stokes equations. We use spherical coordinates (r, θ, φ), where r is the radial distance from the origin, θ the polar angle measured from the z-axis and φ is the azimuthal coordinate starting from the x-axis. The mid-plane of the disc is at the equator $\theta = \frac{\pi}{2}$ and the origin of the coordinates is centred on the star. We work in a coordinate system which rotates with angular velocity

$$\Omega_p = \sqrt{\frac{G(M + m_p)}{a_p^3}} \simeq \sqrt{\frac{GM}{a_p^3}},$$

where M is the mass of the central star and a_p is the semi-major axis of a planet of mass m_p. The gravitational influence of the planet on the disc is modelled as in Kley et al. (2009) using a cubic-potential

of the form

$$\Phi_p = \begin{cases} -\frac{m_p G}{d} & d > r_{sm} \\ -\frac{m_p G}{d} f(\frac{d}{r_{sm}}) & d \leq r_{sm} \end{cases} \tag{1}$$

with $f(\frac{d}{r_{sm}}) = [(\frac{d}{r_{sm}})^4 - 2(\frac{d}{r_{sm}})^3 + 2\frac{d}{r_{sm}}]$;
d is the distance from the disc element to the planet and r_{sm} the smoothing length: $r_{sm} = \alpha_{sm} R_H$, where α_{sm} is a smoothing parameter and R_H is the Hill radius of the planet:

$$R_H = a_p \sqrt[3]{\frac{m_p}{3M}}.$$

Unless specified, we take $\alpha_{sm} = 0.5$ in our simulations. The potential of equation (1) is well suited to 3D simulations (Kley et al. 2009) and different from the typical ϵ-potential used in two-dimensional models:

$$\Phi_p^\epsilon = -\frac{m_p G}{\sqrt{d^2 + \epsilon^2}}. \tag{2}$$

Actually, in two-dimensional models, equation (2) allows us to mimic the average influence that the planet would have on the vertical gas column. A value often used for the smoothing is $\epsilon = 0.7H$, where H is the disc scaleheight, but see Kley et al. (2012) for a more detailed analysis.

To the usual Navier–Stokes equations (see Appendix), we add the equations for the internal energy modelled as in Kley et al. (2009):

$$\begin{cases} \frac{\partial E}{\partial t} + \nabla \cdot (E\boldsymbol{v}) = -p\nabla \cdot \boldsymbol{v} + Q^+ \\ \qquad\qquad\qquad -\nabla \cdot D\nabla T \quad, \\ D = -\frac{\lambda c 4 a_r T^3}{\rho \kappa} \end{cases} \tag{3}$$

where E is the internal energy $E = \rho c_v T$, T is the temperature of the disc and c_v is the specific heat at constant volume. On the right-hand side, the first term denotes the compressional heating, Q^+ the expression for the viscous heating and $D\nabla T$ is the radiative flux.

The diffusion coefficient D is provided by the flux-limited diffusion approach (Levermore & Pomraning 1981) with flux limiter λ[2] (Kley 1989), c is the speed of light, κ the Rosseland mean opacity and a_r the radiation constant. We use the opacity law of Bell & Lin (1994). The viscous heating can be found in Mihalas and Weibel-Mihalas (1984).

The system of equations is closed using an ideal gas EOS: $P = R_{gas}\rho T/\mu$ with mean molecular weight $\mu = 2.3(g\,mol^{-1})$ for standard solar mixture. Taking into account that

$$E = R_{gas}\rho T/\mu(\gamma - 1),$$

this relates to the pressure as

$$P = E(\gamma - 1).$$

In the following, we will use $\gamma = 1.43$, where γ is the adiabatic index. The sound speed differs from the isothermal sound speed by a factor $\sqrt{\gamma}$, that is: $c_s = \sqrt{\gamma P/\rho}$.

---

[2] The expression that we use in the code is

$\lambda = 2/(3 + \sqrt{9 + 10s^2})$

for $s \leq 2$ and

$\lambda = 10/(10s + 9 + \sqrt{81 + 180s})$

for $s > 2$ with $s = \frac{4}{\rho\kappa}\frac{|\nabla T|}{T}$.

We use units such that $G = 1$ and $M = M_\odot = 1$. The orbital period of a planet with semi-major axis $a_p = 1$ is therefore $\tau = 2\pi$. In the following, we normalize the time t by τ, so that t corresponds to the number of orbits of the planet.

3 TRANSITION FROM OUTWARD TO INWARD MIGRATION: TOTAL TORQUE

The aim of this section is to follow the time evolution of the total torque until a stationary situation is reached. The stationary torque is computed for a range of planetary masses with the goal of detecting the mass for which there is a transition from outward to inward migration (i.e. from positive to negative torque). We then compare the transition mass to that predicted in the formula provided by Paardekooper et al. (2011). We consider the disc setting of Kley et al. (2009), namely a disc of mass $M = 0.01\,M_\odot$ with surface density $\Sigma(r) = \Sigma_0 (r/a_J)^{-1/2}$ with $\Sigma_0 = 6.76 \times 10^{-4}$ in code units (2222 kg m^{-2}), initial aspect ratio $h = \frac{H}{r} = 0.05$ and extending from $r_{min} \leq r \leq r_{max}$ with $r_{min} = 0.4$ and $r_{max} = 2.5$ in units of $a_J = 5.2$ au. In the vertical direction, the disc extends from the mid-plane ($\theta \simeq 90°7'$ above the mid-plane, i.e. $\theta \simeq 83°$). We do not study inclined planets orbits therefore we don't need to extend the disc below the mid-plane. We use the boundary conditions explained in the appendix.

Before placing planets in the 3D disc, we bring the latter to radiative equilibrium. Because the disc is axisymmetric in absence of the planet, we model the disc in 2D, with coordinates (r, θ). With our set of parameters, the opacity and a constant viscosity coefficient of 10^{-5} in code units (or 10^{11} m^2 s$^{-1} = 10^{15}$ cm^2 s^{-1}), the equilibrium between viscous heating and radiative cooling reduces the aspect ratio of the disc from the initial value of 0.05 to 0.037 at $r = 1$. Once the 2D equilibrium is achieved, all the gas fields are expanded to 3D. Planets of different masses are then embedded in such an equilibrium disc and held on fixed circular orbits at $r = 1$, $\varphi = \pi$, $\theta = \pi/2$ (mid-plane). Since the frame is corotating with the planet, the planet stays fixed at the corner of eight cells. We compute the torque acting on planets integrating over the whole disc until the torque becomes almost constant (stationary state).

It is common to exclude the inner part of the Hill sphere of the planet from the calculation of the gravitational torque acting on the planet. This procedure allows us to exclude the part of the disc that is accreted by planets that form a circumplanetary disc. However, for small-mass planets that don't have a circumplanetary disc, this prescription is not justified. In addition, in our computations, the cells are symmetrically placed around the planet therefore the torque is not affected by any artificial asymmetry that is sometimes avoided by using a Hill's cut.

In this section, we discuss the total torque without the Hill cut. Unless specified, the total torque Γ_{tot} is normalized with respect to Γ_0 (Lin & Papaloizou 1979):

$$\Gamma_0 = (q/h)^2 \Sigma_p r_p^4 \Omega_p^2, \tag{4}$$

where Σ_p is the disc's surface density at the planet location r_p and q is the mass ratio $q = m_p/M_*$.

The resolution of our computational grid is chosen in order to have in the radial direction n grid-cells in the horseshoe region. The half-width of planet horseshoe region is given in the isothermal disc approximation (Masset, D'Angelo & Kley 2006b) by

$$x_{hs} = 1.16 a_p \sqrt{\frac{q}{h}}. \tag{5}$$

Table 1. Simulations parameters.

Mass ($M_\oplus$)	$(N_r, N_\theta, N_\varphi)$	α_{sm}	n cells in x_{hs}
10	(254, 42, 754)	0.5	4
5	(262, 32, 768)	0.5	3
5	(359, 50, 1068)	0.5	4
3	(350, 42, 1025)	0.5	3
3	(464, 60, 1382)	0.7	4
3	(464, 60, 1382)	0.5	4
3	(464, 60, 1382)	0.3	4
3	(464, 60, 1382)	0.1	4
3	(580, 90, 1727)	0.5	5
2	(568, 90, 1696)	0.5	4
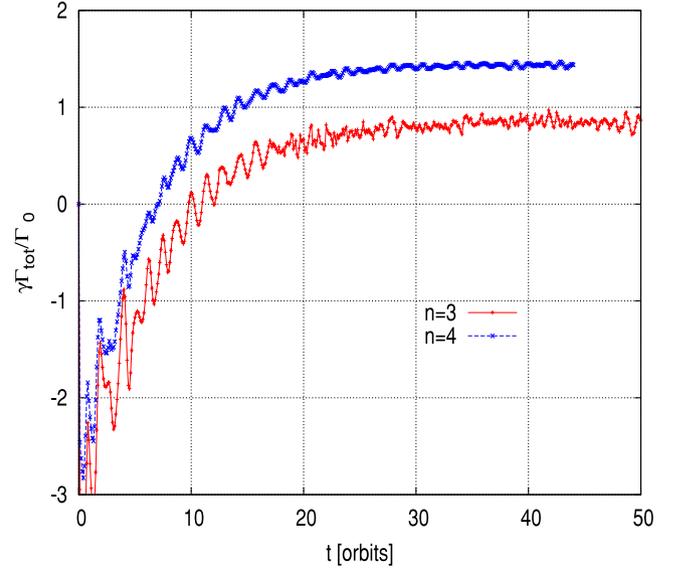
Figure 1. Evolution of the total torque with time for a planet of $5\,M_\oplus$ and two different resolutions corresponding to $n = 3$ and 4 cells in the horseshoe region.

In the following, we consider different masses and different resolutions $(N_r, N_\theta, N_\varphi)$ as shown in Table 1.

A resolution corresponding to $n = 3$ grid-cells in x_{hs} is not enough to properly compute the total torque: we found that the value is underestimated for both the simulations with a planet of $5\,M_\oplus$ (Fig. 1) and $3\,M_\oplus$ (Fig. 2). For a $3\,M_\oplus$ planet, the steady state torque is more negative for $n = 3$ than for $n = 4$ and 5. The choice of $n = 4$ grid-cells in the horseshoe appears to be a good compromise: increasing the resolution further, the total torque does not change any more, so that in the following, we show results obtained for $n = 4$.

For a planet of $2\,M_\oplus$ (also shown in Fig. 2), the steady state torque is negative and of the order of $-2.2\Gamma_0$. Thus, for the considered disc setting (Kley et al. 2009), we can conclude that the transition from positive to negative torque occurs for a planet of mass m_p: $3\,M_\oplus < m_p < 5\,M_\oplus$.

3.1 Role of the potential

In Kley et al. (2009, their fig. 14, top), it is shown that the value of the steady state torque depends on the planetary potential. Deeper potentials enhance the strength of the torque which originates in the vicinity of the planet. For a $3\,M_\oplus$ planet, we have considered different values of the parameter α_{sm} in equation (1). Fig. 3 shows that the deeper the potential is, the more negative the total torque is.
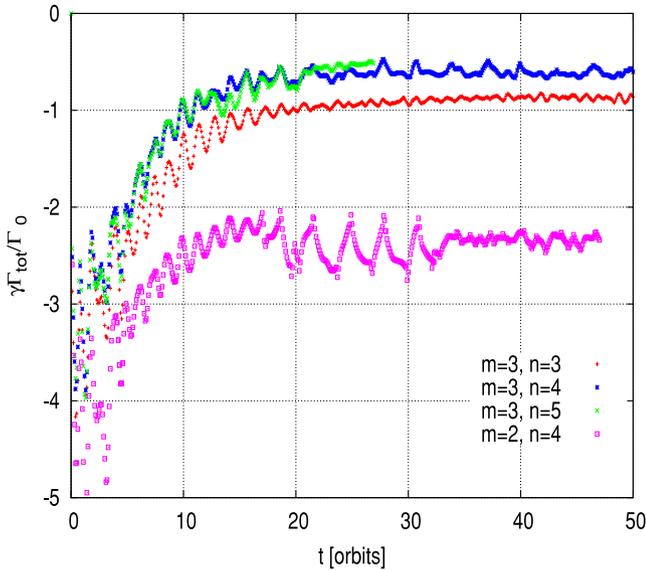
Figure 2. Evolution of the total torque with time for a planet of $3\,M_\oplus$ and three different resolutions corresponding to $n = 3$, 4 and 5 grid-cells in the horseshoe region. Provided that the resolution is at least of four cells in the horseshoe region, the total torque becomes independent from the resolution. The case of a planet of $2\,M_\oplus$ and $n = 4$ is also shown.
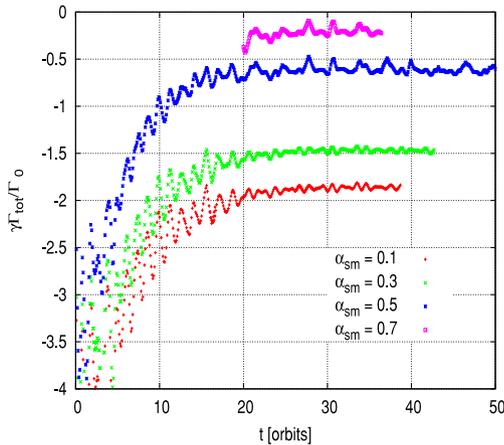

Figure 3. Evolution of the total torque for a planet of $3\,M_\oplus$ and a resolution of $n = 4$ grid-cells in the horseshoe region. Different simulations are run changing the value of the smoothing parameter α_{sm} in the cubic potential (equation 1). Note that the case $\alpha_{sm} = 0.7$ has been restarted from the $\alpha_{sm} = 0.5$ case at 20 orbits. Deeper potentials (smaller values of α_{sm}) give more negative steady state torques.

Apparently, some effects in the close vicinity of the planet produce a negative torque. In fact, we noticed that the steady state total torque for a $3\,M_\oplus$ planet with $n = 4$ becomes positive if a Hill's cut is applied.

3.2 Comparison with analytic formula

It is interesting to compare our results to those of Paardekooper et al. (2011) applying their formula to our disc parameters. We recall that it captures the behaviour of the torque caused by Lindblad resonances and the horseshoe torque on low-mass planets embedded in 2D gaseous discs in the presence of viscous and thermal diffusion. The validity of this formula in the case of fully radiative 3D simulations has been checked in Bitsch & Kley (2011), showing
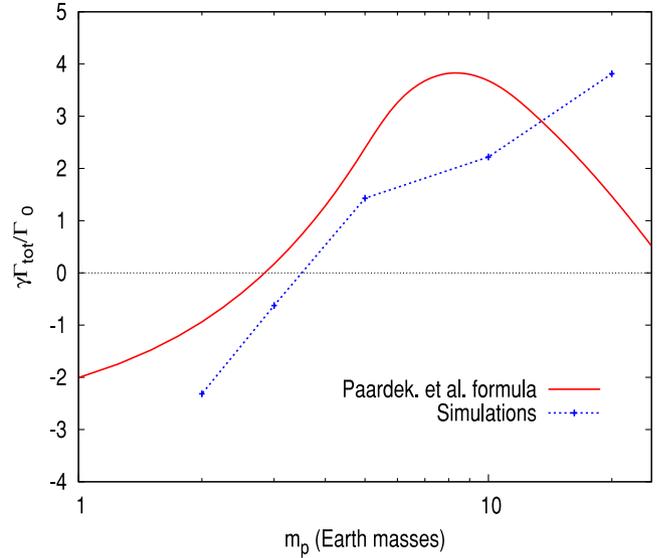
Figure 4. Values of the steady state torque obtained with FARGOCA simulations for planets of different masses. For all the cases, the resolution corresponds to $n = 4$ grid-cells in the horseshoe region and the smoothing parameter is $\alpha_{sm} = 0.5$. For comparison, the values of the torque provided by the Paardekooper et al. (2011) formula are plotted. The values of the torque for a planet of $20\,M_\oplus$ are presented in Fig. A2.

that the formula predicts a torque that is a factor of $3-4$ smaller than that observed in the simulations of planets in the range of $20\,M_\oplus < m_p < 30\,M_\oplus$.

In Fig. 4, we compare the results of our simulations with the values provided by the Paardekooper et al. (2011) formula at $r = 5.2$ au ($r = 1$ in code units). We recall that in the Paardekooper et al. (2011) formula, the whole disc enters in the computation of the total torque so that no Hill cut should be applied in the numerical simulations as we did. A trend towards more negative torque values appears in our data when decreasing the planetary mass.

4 A FINE DESCRIPTION OF THE NEIGHBOURHOOD OF THE PLANET

4.1 Radial torque

In order to study the contribution to the torque in the close vicinity of the planets, we show the radial torque density $\Gamma(r)$. The integral of $\Gamma(r)$ on the radial coordinate provides the total torque Γ_{tot} discussed in the previous section as

$$\Gamma_{tot} = \int_{r_{min}}^{r_{max}} \Gamma(r)\, dr. \qquad (6)$$

Fig. 5 shows the radial torque density normalized with respect to Γ_0, for the set of simulations shown in Table 1 with a resolution corresponding to $n = 4$. We have also added the results obtained for a simulation with a $2\,M_\oplus$ planet for the adiabatic case, i.e. considering in the RHS of the energy equation (3) only the compressional heating term. The simulation is run with an aspect ratio $H/r = 0.037$ (i.e. the value obtained for the radiative equilibrium at $r = 1$) and the same parameters as the case of a $2\,M_\oplus$ planet for $n = 4$. The torque $\Gamma(r)$ for the adiabatic case is shown at a time of 40 orbits for which the total torque has reached a stationary value. Different considerations can be done on Fig. 5 as follows.
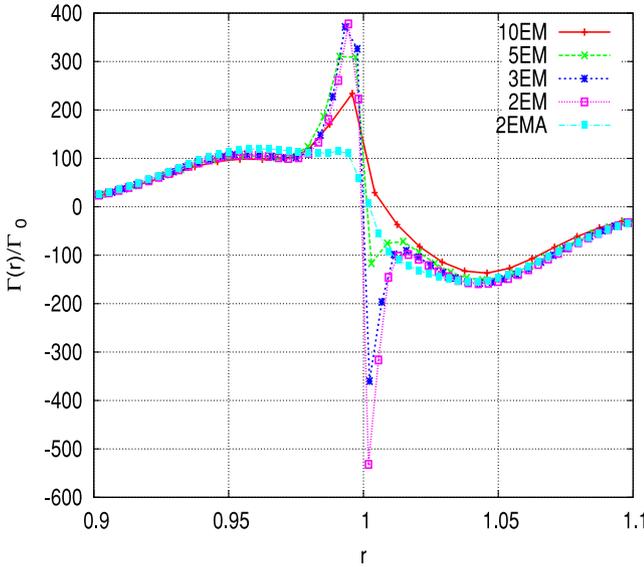
Figure 5. Radial torque density normalized with respect to Γ_0. The Lindblad torque scales with the square of the mass ratio q, while unexpected contributions come from the close vicinity of the planets for $m_p < 10\,M_\oplus$. For comparison the radial torque density obtained for an adiabatic simulation is shown.

(i) The Lindblad torque scales as expected (Goldreich & Tremaine 1980; Paardekooper et al. 2010) with Γ_0, i.e. with the square of the mass ratio q.

(ii) Compared with the adiabatic case, where the component of the corotation torque due to the temperature gradient saturates, we notice that the total torque acting on a $m_p = 10\,M_\oplus$ has a positive contribution just inside $r = 1$; also a small torque excess is observed for $r > 1$. Both features are expected (Paardekooper & Mellema 2006) in radiative discs as a result of the heating and cooling process of the gas librating in the horseshoe region leading to a positive total torque.

(iii) The corotation torque is expected to scale with Γ_0. At $r < 1$, we observe a positive spike due to the entropy-related part of the corotation torque (non-linear contribution or horseshoe drag). Decreasing the planetary mass, we expect that the horseshoe drag tends towards the linear corotation torque. Instead, in Fig. 5, we observe that the positive contribution remains when decreasing the planetary mass.

(iv) A new and totally unexpected feature appears for $r > 1$. We observe a negative spike which is not seen for $m_p \geq 10\,M_\oplus$ and which becomes more and more important when decreasing the mass of the planet.

(v) The positive and negative spikes contributions appear to be asymmetric, the negative spike providing a larger contribution which is responsible for the negative total torque, i.e. for the transition from outward to inward migration.

At the light of this picture, it is easy to see that the exclusion of the inner part of the Hill sphere of the planet in the torque computation would reduce mainly the effect of the negative spike which is closer to the planet location than the positive spike, which will then 'survive' the Hill cut. This is shown in Fig. 6 where the blue curve is similar to the green one except that a Hill's cut has been applied. This fact explains the change of sign of the total torque for the $3\,M_\oplus$ case mentioned before. Moreover, the negative spike appears to be more important for deeper potentials (Fig. 6) thus explaining results of Fig. 3.
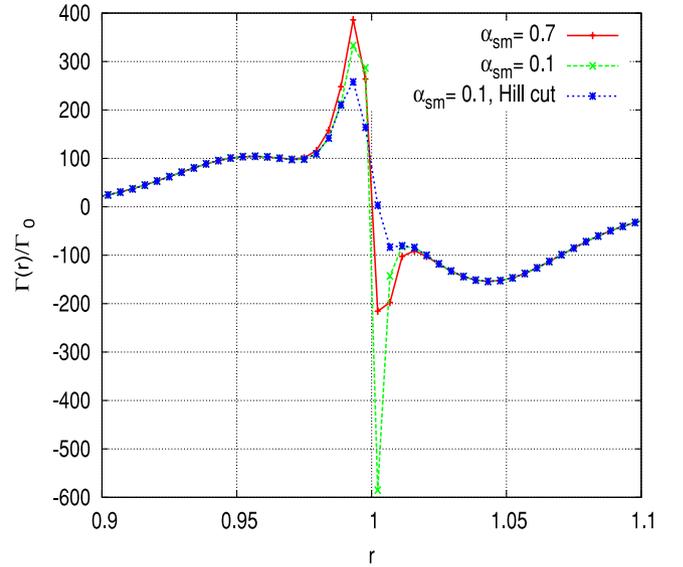

Figure 6. Radial torque density for a planet of $3\,M_\oplus$ and resolution $n = 4$, using the cubic potential (equation 1) with two different values of the smoothing parameter: $\alpha_{sm} = 0.1$ and 0.7. The contribution of the negative spike observed for $r > 1$ is more important for deeper potentials. For comparison, the case $\alpha_{sm} = 0.1$ is plotted considering the Hill cut.

4.2 Local dynamics

In order to understand the origin of these torques contributions together with their asymmetry, we investigate the dynamics in the vicinity of the planet.

Figs 7 and 8 show the contributions of individual mid-plane grid-cells to the torque on the planets for, respectively, a $10\,M_\oplus$ and a $2\,M_\oplus$ planet. The torque is constructed by adding to each grid-cell the contribution of the symmetric cell with respect to the planet location; for a planet in r_p, θ_p, φ_p, we have on a coordinate r, φ

$$\tilde{\Gamma}_{\theta_p}(r, \varphi) = \Gamma_{\theta_p}(r, \varphi) + \Gamma_{\theta_p}(r, 2\pi - \varphi), \qquad (7)$$
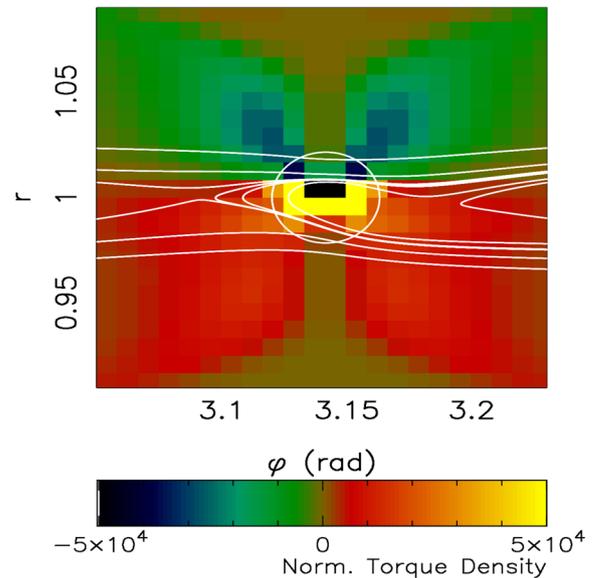
Figure 7. Normalized torque density $\tilde{\Gamma}_{\theta_p}$ acting on a planet of $10\,M_\oplus$ caused by the density in each individual mid-plane grid-cell as defined in equation (7). Some streamlines are shown by white curves. The circle around the point $(\pi, 1)$ shows Hill's sphere of the planet.
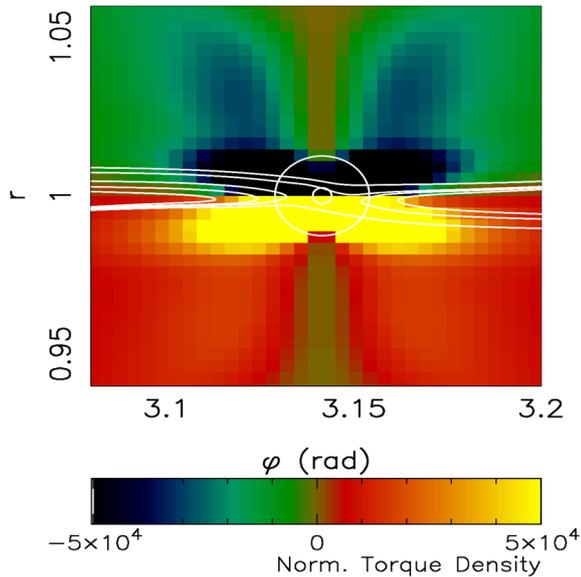
Figure 8. Same as Fig. 7 but for a planet of $2\,M_\oplus$. The small circle around the point $(\pi, 1)$ shows Bondi's sphere of the planet.

where $\Gamma_{\theta_p}(r, \varphi)$ is a volume torque density, i.e. it is the torque exerted on the planet by the mass density ρ placed at (r, φ, θ_p). The torque density has been normalized with respect to Γ_0.

The quantity $\tilde{\Gamma}$ is symmetric with respect to φ_p, so that only the left side of Figs 7 and 8 ($\varphi < \varphi_p$) can be taken into account to estimate global effects. A positive (negative) value of $\tilde{\Gamma}_{\theta_p}(r, \varphi)$ in the whole interval $0 < \varphi < \pi$ corresponds to positive (negative) radial density torque on the mid-plane. We notice that the change of sign of $\tilde{\Gamma}_{\theta_p}(r, \varphi)$ in the vicinity of the planet location that we observe in Figs 7 and 8 is in agreement with Fig. 5 where the radial torque density has been obtained considering also the contribution of the grid-cells in the vertical direction and not only on the mid-plane as given by equation (7).

Therefore, it is justified to search for the origin of the negative spike at $r > 1$ analysing the values of different gas quantities only on the mid-plane. At first, we notice in Fig. 8 strong negative (positive) values of $\tilde{\Gamma}_{\theta_p}(r, \varphi)$ at $r > 1$ ($r < 1$) in the vicinity of the planet location that are not observed in Fig. 7.

The circle around the point $(\pi, 1)$ shows Hill's sphere of the planet. In Fig. 8, we have also plotted Bondi's sphere of the planet, with the Bondi radius defined by

$$R_B = \frac{Gm_p}{c_s^2}. \tag{8}$$

It appears clearly that the region concerned by the positive and negative torque excesses is larger than Bondi's sphere. From the streamlines overplotted, we can observe that many streamlines pass in the vicinity of the planet outside of Bondi's sphere.

4.3 Density analysis

Looking carefully at the density plot (Fig. 9, top panel, mid-plane values are shown), we see that the density distribution around a $2\,M_\oplus$ planet is asymmetric. In particular, just outside the planet orbit ($r > 1$), the density is larger at $\varphi < \varphi_p$ than symmetrically with respect to φ_p at $\varphi > \varphi_p$. This gives the negative contribution to the total torque in Fig. 8. Instead, just inside the planet orbit ($r < 1$), the density is larger at $\varphi > \varphi_p$ than at $\varphi < \varphi_p$. This gives
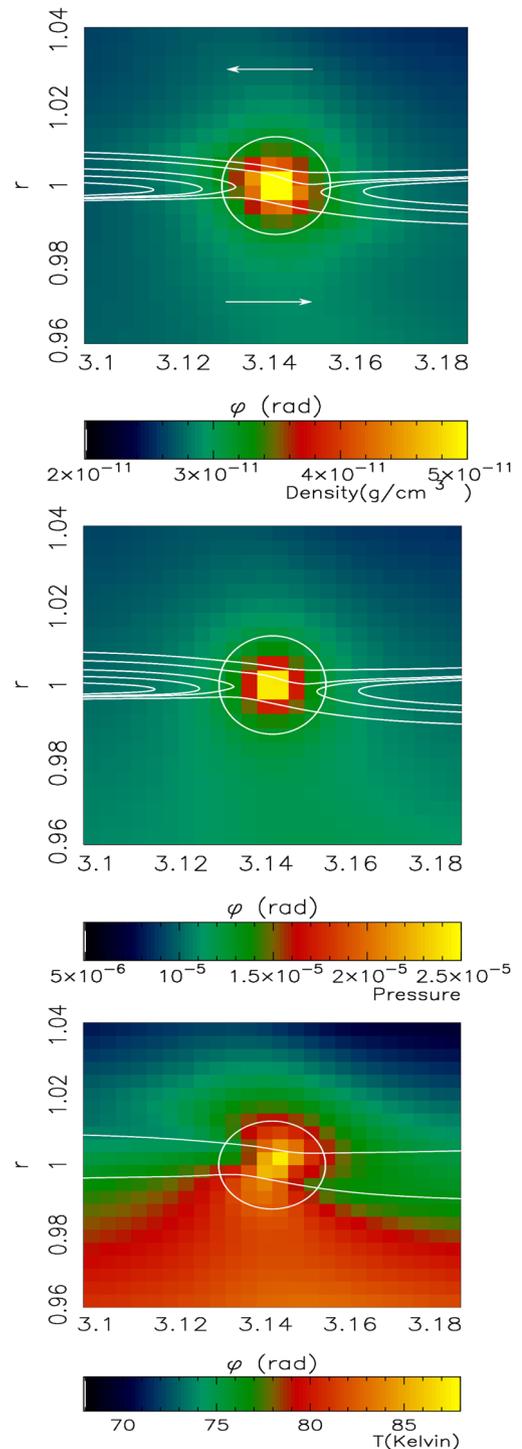

Figure 9. Mid-plane plots for a $2\,M_\oplus$ planet. Top panel: density field, middle panel: pressure field, bottom panel: temperature field. Some streamlines are shown by white curves. The arrows in the top panel indicate the flow circulation: from right to left for $r > 1$ and from left to right for $r < 1$. Two streamlines are shown in the bottom panel passing through points symmetric with respect to the planet position: $r - r_p = 5.5 \times 10^{-3}$, $\varphi - \varphi_p = -5.5 \times 10^{-3}$ (top), $r - r_p = -5.5 \times 10^{-3}$, $\varphi - \varphi_p = 5.5 \times 10^{-3}$ (bottom).

the positive contribution to the total torque in Fig. 8. The same is observed for higher planet masses (Figs 10 and 11).
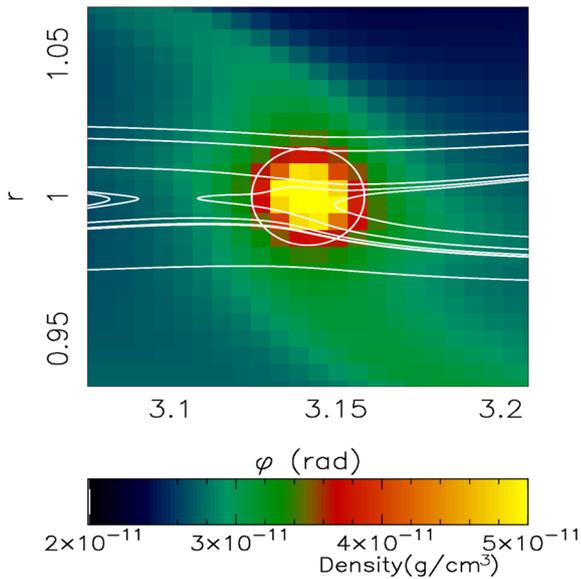
We remark that, because the gas circulates from right to left for $r > 1$ and from left to right for $r < 1$, both density enhancements
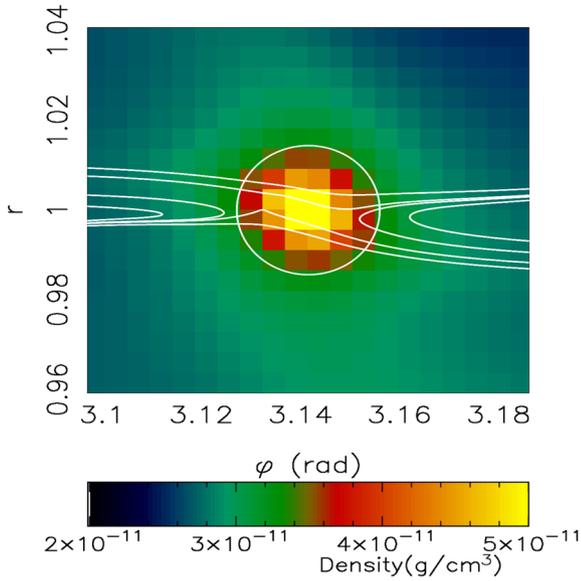
Figure 10. Mid-plane density field for a $3\,M_\oplus$ planet (resolution $n = 4$, $\alpha_{sm} = 0.5$).
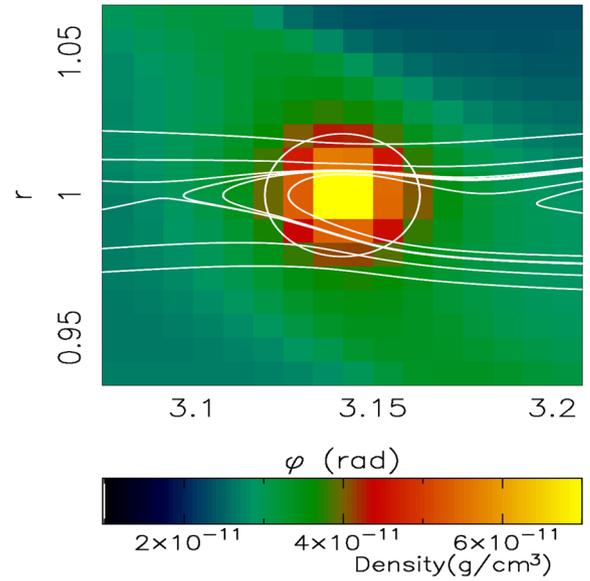
Figure 12. Mid-plane density field for a $10\,M_\oplus$ planet (resolution $n = 4$, $\alpha_{sm} = 0.5$).

Figure 11. Mid-plane density field for a $5\,M_\oplus$ planet (resolution $n = 4$, $\alpha_{sm} = 0.5$).

occur downstream relative to the encounter of the gas with the planet.

In Fig. 9, middle panel, we see that the vicinity of the planet is a region of high pressure and that the pressure field is azimuthally perfectly symmetric. As a consequence, the EOS implies that variations of density and temperature with respect to symmetry are anticorrelated (see Fig. 9, bottom panel).

We explain what is observed as follows: when the gas goes through the high-density and high-pressure region close to the planet, it is compressed and its temperature increases (adiabatic heating). If the EOS were adiabatic, the temperature, density and pressure would come back to the original values after leaving the planet vicinity. But, when radiative transfer is included, the gas cools during the entire encounter with the planet, i.e. when it is hotter than the unperturbed temperature. Consequently, as it comes

back to the original pressure, the gas is colder after the encounter with the planet than it was before the encounter, because it has lost internal heat. This leads to the formation of a cold and therefore dense finger downstream relative to the planet location, namely ahead of the planet just inside of its orbit, and behind the planet just outside of its orbit.

In the case of a $5\,M_\oplus$ planet (Fig. 11), we notice only one stagnation point at $\varphi < \varphi_p$ at r slightly smaller than 1. Therefore, also some libration streamlines pass through the high-density and high-pressure region and provide, through the same mechanism, an excess of density after the encounter with the planet for $\varphi > \varphi_p$, $r < 1$. The same occurs for the planet of $10\,M_\oplus$ (Fig. 12). Therefore, the positive contribution to the torque at $r < 1$ seems to be due to two effects: the first one is due to the libration and circulation streamlines passing through the high-pressure region as we just described. The second effect is due to horseshoe streamlines that pass further from the planet and do not heat up significantly during the encounter, thus bringing gas from a colder to a hotter part of the disc as described by Paardekooper & Mellema (2006).

Moreover, the distribution of the gas density around the planet observed at $10\,M_\oplus$ appears to be more symmetric than for smaller masses. We notice that although some circulation streamlines pass through the high-density region, their distance from the planet is larger than for smaller masses. As we will show in the next section, the effect of adiabatic heating and radiative cooling and therefore the downstream density enhancement vanishes with increasing distance from the planet.

At our knowledge, this phenomenon was not observed in previous 2D simulations probably because of the smoothed potential (equation 2) which is used in 2D simulations to soften the effect of the vertical gas column as explained in the Introduction. In the following section, we show results obtained with 2D simulations in which we use the cubic potential and a simple cooling prescription in which the cooling time appears as a parameter. The aim is to recover the proposed mechanism and to study its characteristics as a function of the cooling properties of the disc.

5 2D SIMULATIONS

In order to better understand the basic physics at play around a small-mass planet, we have performed 2D simulations. The potential of the planet was smoothed like in 3D simulations, given by equation (1); by doing so, we do not pretend to model accurately a thick disc, but to study the dynamics in the mid-plane.

Having only two dimensions allows a higher resolution, but the radiative cooling cannot be modelled accurately. This turns out to be an advantage, as we can use a simplified, controlled treatment of the heating/cooling processes. We use the following energy equation:

$$\frac{\partial E}{\partial t} + \nabla \cdot (E\boldsymbol{v}) = -p\nabla \cdot \boldsymbol{v} - c_{\mathrm{v}}\Sigma\frac{T - T_0}{\tau_{\mathrm{c}}}, \tag{9}$$

where $\Sigma = \int \rho\, \mathrm{d}z$ is the surface density, τ_{c} is the cooling time and T_0 is the initial temperature, defined as $T_0(r) = (GM_*/r)h^2$. In short, this is an adiabatic EOS, with exponential damping of the temperature perturbations. Note that we do not consider the viscous heating term as in equation (3) since the main source of heating close to the planet is the compressional heating.

We have done two sets of simulations on a computational domain (r, θ) consisting of an annulus of the protoplanetary disc extending from r_{min} to r_{max} with $r_{\mathrm{min}} = 0.6$, $r_{\mathrm{max}} = 1.651\,85$ on a grid of $N_r \times N_\theta = 568 \times 3392$ grid-cells for set A; $r_{\mathrm{min}} = 0.8$, $r_{\mathrm{max}} = 1.325\,925$ on a grid of $N_r \times N_\theta = 568 \times 6684$ grid-cells for set B. Both sets of simulations have squared grid-cells of side 1.85×10^{-3} (set A) and 9.25×10^{-4} (set B) at the planet location, $h = 0.05$ and a constant viscosity coefficient of 10^{-5} in code units (or $10^{11}\,\mathrm{m^2\,s^{-1}} = 10^{15}\,\mathrm{cm^2\,s^{-1}}$). Fig. 13, top panel, shows (set B) the perturbed temperature T/T_0 in the neighbourhood of a 2 Earth mass planet after 60 orbits, with $\tau_{\mathrm{c}} = (2/\Omega_{\mathrm{p}})(r/r_{\mathrm{p}})^2$. Inside the Hill sphere of the planet, compressional heating takes place. However, along the outgoing streamlines, the temperature is significantly colder than before, in agreement with what was seen in 3D. This happens because the expansion cools a gas that has already lost some internal energy due to the radiative cooling. The temperature then slowly comes back to the unperturbed one (following the prescribed exponential damping). The colder finger can be traced as well in the density plot (Fig. 13, middle panel), through a high-density finger which gives a torque contribution as shown in Fig. 13, bottom panel.

The high resolution allows us to study the shape of this diagonal cold finger. In Fig. 13, the boundary $T = T_0$ follows almost a straight line passing through the planet, making an angle $\eta \sim 55°$ with the radial direction. The relative velocity with respect to the planet of a particle orbiting around the star at a distance $r_{\mathrm{p}} + \delta r$ being about $\delta r \times \frac{3}{2}\frac{\Omega_{\mathrm{p}}}{r_{\mathrm{p}}}$, this line corresponds to a time $\delta t = \frac{2\tan\eta}{3\,\Omega_{\mathrm{p}}} \propto \tau_{\mathrm{c}}$ after the conjunction with the planet, that is after the maximal compression. In simulations where the cooling time is different, the angle η changes accordingly, as can be seen in Fig. 14.

This shows that the particular structure we have discovered around low-mass planets (this diagonal cold finger) is robust against the processes of heating and cooling. Provided the EOS is not purely adiabatic, it will appear.

Since the gas cools as it moves through the planet potential, the mechanism is optimally effective when the cooling time is of the same order as the dynamical time. Actually, in Fig. 14, top panel ($\tau_{\mathrm{c}} = 10/\Omega_{\mathrm{p}}$), the diagonal cold finger is weaker and appears farther from the planet with respect to the cases with $\tau_{\mathrm{c}} = 2, 1/\Omega_{\mathrm{p}}$. We have obtained a very weak cold finger for a simulation run with
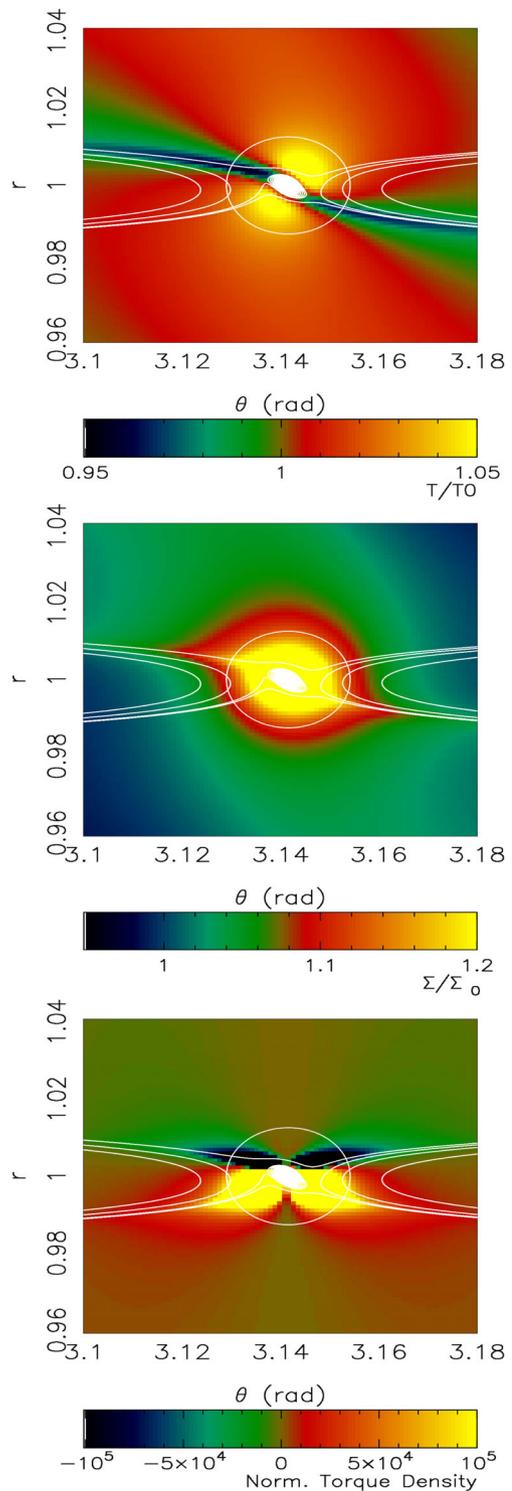
Figure 13. 2D simulation: perturbed temperature (top panel), perturbed density (middle panel) and normalized torque density (bottom panel) around a $2\,\mathrm{M}_\oplus$ planet after 60 orbits. The energy equation is given by equation (9) with $\tau_{\mathrm{c}} = \sim 2/\Omega_{\mathrm{p}}$. About half a cooling time after the maximum of the compression (at conjunction with the planet), the gas becomes cooler than initial, making a diagonal cold finger (in blue, middle panel). The cold finger of gas corresponds to a denser diagonal finger. The comparison with the 3D simulations results of Figs 8 and 9 shows that the same mechanism acts both in the 2D and 3D case.
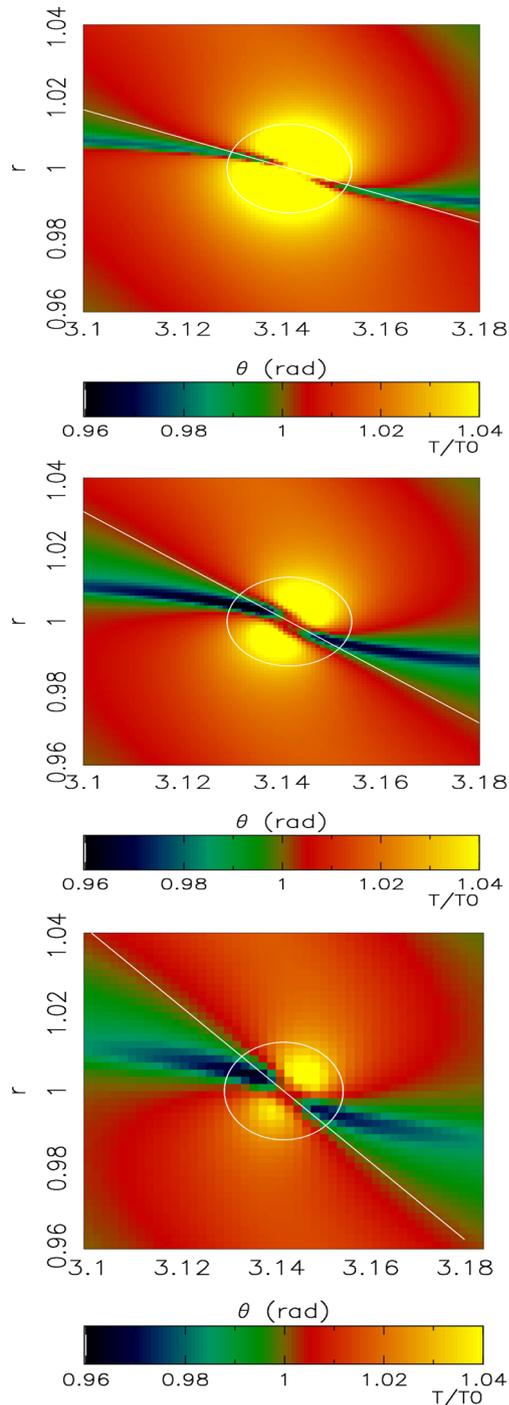
Figure 14. 2D simulation: perturbed temperature variations around a $2\,\mathrm{M}_\oplus$ planet after 10 orbits with three different values for the cooling time: from top to bottom $\tau_c = \{10, 2, 1\}/\Omega_p$. The shape of the cold region after encounter with the planet changes, as the coldest temperature corresponds to about 1 cooling time after the conjunction with the planet. The boundary $T = T_0$ follows almost a straight line (white line on the plots) passing through the planet. The line forms an angle η with the radial direction, scaling according to $\tan(\eta) \sim \tau_c$ (see text). The resolution is that of set B (see text) for the top and middle panels and that of A for the bottom one.

$\tau_c = 50/\Omega_p$ while the phenomenon didn't appear for a simulation run with $\tau_c = 100/\Omega_p$.

The comparison with the 3D radiative cooling rate is not so straightforward. If we consider the radiative cooling time-scale as

defined in Bitsch & Kley (2010),

$$\tau_{\mathrm{rad}} = \frac{H^2}{D/c_v\rho}, \tag{10}$$

where D is the diffusion coefficient of equation (3) with $\lambda = 1/3$. The value of $\tau_{\mathrm{rad}}\Omega_p$ is about 100 at $r = r_p$ and turns out to decrease for $r < r_p$ (see Bitsch & Kley 2010, fig. A.1 for the same disc parameters as in our simulations). The phenomenon should therefore be even more effective going towards the inner part of the disc.

It should also be noted that the observed phenomenon is not in contradiction with the usual thermal part of the corotation torque (Paardekooper & Mellema 2006, 2008; Baruteau & Masset 2008). In Fig. 15, top panel, the temperature variations are shown after 35 orbits, with $\tau_c = 2/\Omega_p$, with a larger range in the azimuthal direction. The hot and cold plumes expected in the horseshoe region are present along streamlines that did a U-turn far enough from the planet to avoid being heated significantly by compression (which would have made them lose internal heat). However, the cold finger is also present, and shows actually a larger temperature variation than the plumes. For comparison, we show (Fig. 15, bottom panel), the same simulation with a pure adiabatic EOS (no cooling) after 35 orbits. The torque in the horseshoe region has not yet reached saturation so that hot and cold plumes are still present. The horseshoe region appears to be thinner than in the radiative case and circulation streamlines that pass through the high-pressure region close to the planet do not create any cold finger. Actually, after the encounter with the planet, the expansion cools the gas back at the unperturbed temperature.

In order to see the cold finger, one needs gas passing through the high-pressure region around the planet, without being bound to it. On the one hand, the high-pressure region around the planet typically has the size of its potential well: the Hill radius R_H which is proportional to $m_p^{1/3}$. On the other hand, an upper estimate of the region bound to the planet is the Bondi radius which is proportional to m_p. Therefore, the cold finger can only appear if the Hill radius is significantly larger than the Bondi radius. In our case,
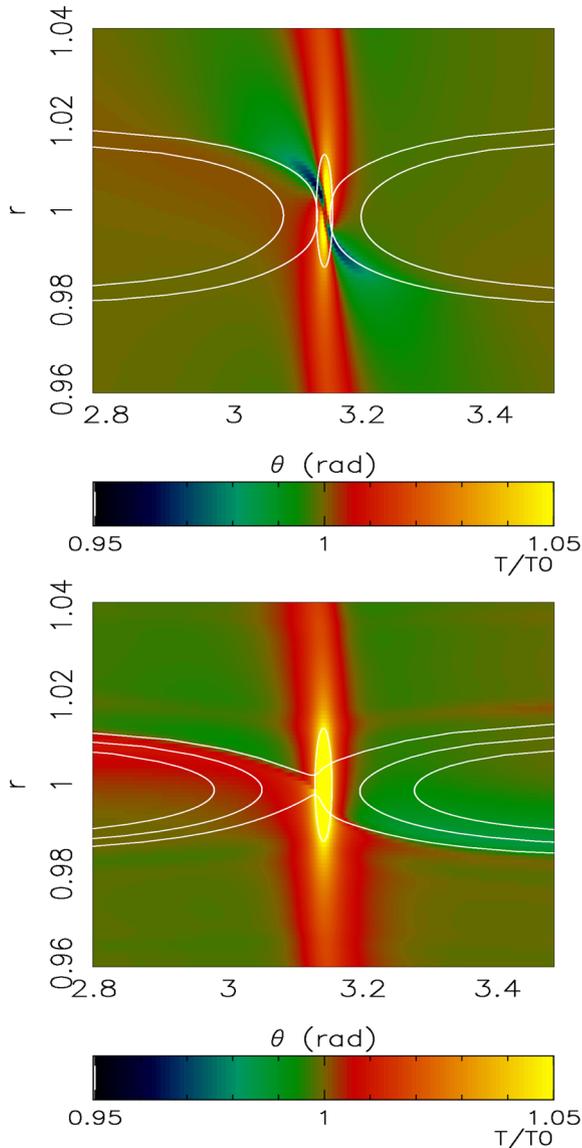
$$\frac{R_B}{R_H} = \frac{(m_p/7.1\,\mathrm{M}_\oplus)^{2/3}}{(a/5.2\,\mathrm{au})(T/75\,\mathrm{K})}, \tag{11}$$

which implies that $R_B < R_H$ for $m_p < 7.1\,\mathrm{M}_\oplus$. Therefore, the cold finger effect was not prominent in previous 3D simulations because they have been done for planets more massive than $5\,\mathrm{M}_\oplus$ (Paardekooper & Mellema 2006, 2008; Kley et al. 2009).

Concerning 2D simulations, this phenomenon was not observed before because it is common to use a smoothing length of the order of the scale height of the disc (see Fig. 16). In fact, for a typical aspect ratio of 5 per cent, the standard smoothing length $\epsilon = 0.6H$ is larger than the Hill radius for planets smaller than $27\,\mathrm{M}_\oplus$. Obviously, with a smoothing length comparable or larger than the Hill radius it is not possible to simulate correctly the dynamics of the gas between the Bondi radius and the Hill radius. In particular, the pressure maximum is strongly weakened. We remind the reader that to see the cold finger effect in 2D simulations, we used a smoothing length that is a fraction of the Hill radius.
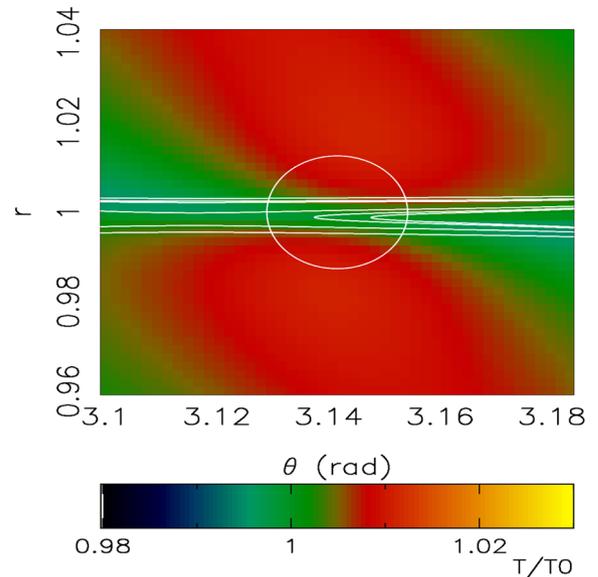
6 ON THE ASYMMETRY OF THE COLD FINGERS

We know from the measures of the radial torque density (Fig. 5) that the cold finger appears to be asymmetric with a larger contribution at $r > 1$ that is responsible for the negative total torque.
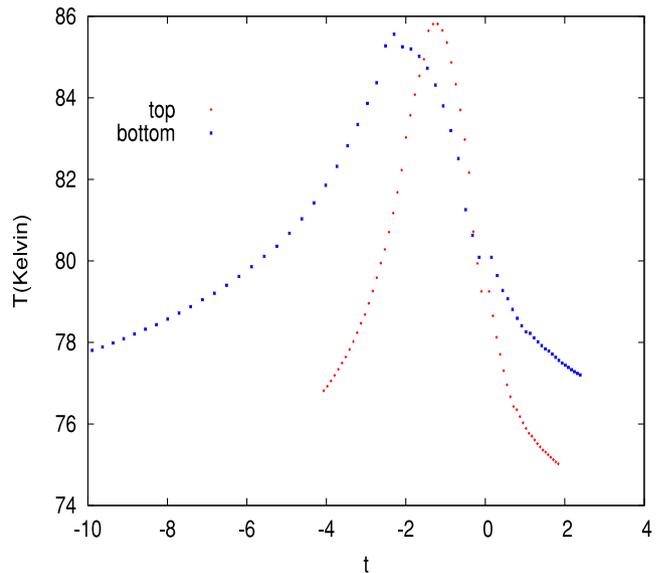
Figure 16. 2D simulation: perturbed temperature around a $2\,M_\oplus$ planet after 60 orbits, with $\tau_c = 4/\Omega_p$ and standard ϵ-potential with smoothing length $\epsilon = 0.6H$, where $H/r = 0.05$.

Figure 15. 2D simulation. Top panel: perturbed temperature around a $2\,M_\oplus$ planet after 35 orbits, with $\tau_c = 2/\Omega_p$. Streamlines making a U-turn far enough from the planet to be heated by compression are associated to the usual thermal part of the corotation torque. Streamlines passing in the close vicinity of the planet show the cold finger resulting from compressional heating and radiative cooling. Bottom panel: perturbed temperature around a $2\,M_\oplus$ planet after 35 orbits in the adiabatic case. The torque in the horseshoe region has not yet reached saturation so that hot and cold plumes are still present but no cold finger structure appears in this case.

Figure 17. Variation of the temperature along the two streamlines of Fig. 9. The label 'top' corresponds to the streamline passing through $r - r_p = 5.5 \times 10^{-3}$, $\varphi - \varphi_p = -5.5 \times 10^{-3}$, 'bottom' to the one passing through $r - r_p = -5.5 \times 10^{-3}$, $\varphi - \varphi_p = 5.5 \times 10^{-3}$. Positive times correspond in both cases to the part of the streamline downstream relative to the encounter of the gas with the planet.

In Fig. 17, we show the variation with time of the temperature associated to the two streamlines shown in Fig. 9, bottom panel. We recall that the gas moves from right to left for the top streamline and from left to right for the bottom one. In both cases, the initial condition is chosen after the encounter with the planet: positive (negative) times in Fig. 17 correspond to the part of the streamline downstream (upstream) relative to the encounter of the gas with the planet. The gas associated to the top streamline (in Fig. 9, bottom panel) has a larger relative temperature variation with respect to the bottom one (in Fig. 9, bottom panel). Precisely, 75/76.8 for top one instead of 77/77.75 for the bottom one. Therefore, the density enhancement for $r > 1$ has to be sharper than for $r < 1$.

We consider the following explanation for the asymmetry: the flow is slightly sub-Keplerian due to the pressure gradient in the disc; therefore, the stagnation points are located at $r < r_p$ and as a consequence circulation streamlines pass closer to the planet location for $r > r_p$ than for $r < r_p$.

In order to test this hypothesis, we have run a 2D simulation with constant surface density $\Sigma = \Sigma_0$ and disc height $H(r) = h_0 r^{3/2}$ in order to have constant temperature with respect to r, so that the disc is Keplerian since the radial pressure gradient is null. Fig. 18 shows the ratio T/T_0. When compared to Fig. 13, the hot regions inside the Hill sphere (in yellow) appear more symmetric with respect to the
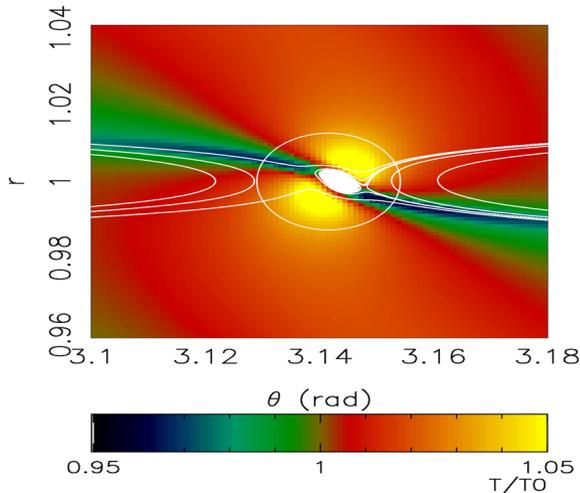
Figure 18. 2D simulation: perturbed temperature around a $2\,M_\oplus$ planet after 60 orbits for a simulation in which the gas has Keplerian speed, the surface density and the temperature are initially constant with respect to r.

planet position but the cold finger is now slightly colder for $r < r_\mathrm{p}$ than for $r > r_\mathrm{p}$. We have to carefully investigate the topology of the streamlines around the planet to understand why the cold finger is not symmetric when the gas has Keplerian speed. The streamlines appear to be sensitive on tiny variations in the velocity field and not symmetric: in particular, one streamlines goes around the planet, and leaves it on the bottom right. As a consequence, the cold finger is slightly colder on the bottom right than on the top left. The reason is that the viscous evolution of the disc makes the gas drift inwards. Note that the variation of the angular momentum is proportional to the radial gradient of $\sqrt{r}\,\Sigma\nu$ so that, for constant viscosity, it is null for $\Sigma \propto 1/\sqrt{r}$, as considered in the previous set of 2D simulations.

It is clear that a good knowledge of the flows around the planet allows us to determine the characteristics of the cold finger. Further studies are necessary to model the dynamics in the close vicinity of the planet. This actually may well determine the migration direction and rate for small-mass planets.

7 CONCLUSION

Using 3D hydrodynamical simulations including radiative transfer, we have computed the torque acting on small-mass planets kept on fixed orbits in the aim of finding the critical mass for which the positive contribution of the corotation torque becomes smaller than the Lindblad torque. While we were expecting to observe that the positive corotation torque fades away for decreasing mass of the planet, we found a new and unexpected feature: a negative contribution to the torque that is not seen for planetary masses larger than $m_\mathrm{p} \gtrsim 5\,M_\oplus$. We explain this phenomenon observed in viscous discs[3] as follows. Small-mass planets do not have a circumplanetary disc, but their gravitational force still increases the pressure and temperature in their neighbourhood. Looking at density and temperature fields, it appears that some circulating or even some librating streamlines go through pressure increase as they encounter the planet. If the EOS is locally isothermal or purely adiabatic, the temperature, density and pressure are identical before and after this

---

[3] We do not refer to the non-viscous case nor to the limit of vanishing viscosity.

pressure peak. However, if radiative transfer is included, the gas is cooler, thus denser, after the encounter with the planet. This leads to the formation of a cold and dense finger ahead of the planet just inside of its orbit, and behind the planet just outside of its orbit, outside of the horseshoe region. This phenomenon, which we have recovered with two-dimensional high-resolution simulations, explains the unexpected negative contribution observed on the torque just outside the planet orbit in 3D simulations.

At our knowledge, the cold finger was not observed in previous numerical computations. We understand that, in order to have a torque contribution related to the cold finger in viscous discs, the following conditions must be satisfied:

(i) planets have to be small enough for their Hill radius to be significantly larger than their Bondi radius,

(ii) the EOS must be non-isothermal neither adiabatic, with an appropriate cooling time,

(iii) the planetary potential has to be close to the real one, for example the cubic potential introduced in Kley et al. (2009) suited to 3D simulations.

The cold finger turns out not to be symmetric being more pronounced behind the planet with our standard disc's parameters, and it appears to be responsible for the transition from outward to inward migration as the planet mass decreases. However, this asymmetry is very sensitive to the properties of the flow around the planet. In particular, we found a positive total torque in a disc with flat surface density and temperature profile. Therefore, for specific disc properties, Earth-sized planets could still migrate outwards, even when the usual thermal contribution to the corotation torque fades. This enlightens the importance of the cold finger, and advocates for future studies of this new torque contribution.

REFERENCES

Baruteau C., Masset F., 2008, ApJ, 672, 1054
Baruteau C., Fromang S., Nelson R. P., Masset F., 2011, A&A, 533, A84
Bell K. R., Lin D. N. C., 1994, ApJ, 427, 987
Bitsch B., Kley W., 2010, A&A, 523, A30
Bitsch B., Kley W., 2011, A&A, 536, A77
Cresswell P., Dirksen G., Kley W., Nelson R. P., 2007, A&A, 473, 329
Goldreich P., Tremaine S., 1980, ApJ, 241, 425
Guilet J., Baruteau C., Papaloizou J. C. B., 2013, MNRAS, 430, 1764
Kley W., 1989, A&A, 208, 98
Kley W., Crida A., 2008, A&A, 487, L9
Kley W., Bitsch B., Klahr H., 2009, A&A, 506, 971
Kley W., Müller T. W. A., Kolb S. M., Benítez-Llambay P., Masset F., 2012, A&A, 546, A99
Levermore C. D., Pomraning G. C., 1981, ApJ, 248, 321
Lin D. N. C., Papaloizou J., 1979, MNRAS, 186, 799
Lyra W., Paardekooper S.-J., Mac Low M.-M., 2010, ApJ, 715, L68
Masset F. S., 2000a, A&AS, 141, 165
Masset F. S., 2000b, in Garzón G., Eiroa C., de Winter D., Mahoney T. J., eds, ASP Conf. Ser. Vol. 219, Disks, Planetesimals, and Planets. Astron. Soc. Pac., San Francisco, p. 75
Masset F. S., 2002, A&A, 387, 605

Masset F. S., Casoli J., 2009, ApJ, 703, 857
Masset F. S., Casoli J., 2010, ApJ, 723, 1393
Masset F. S., Morbidelli A., Crida A., Ferreira J., 2006a, ApJ, 642, 478
Masset F. S., D'Angelo G., Kley W., 2006b, ApJ, 652, 730
Mihalas D., Weibel-Mihalas B., 1984, Foundations of Radiation Hydrodynamics. Dover Press, New York
Morbidelli A., Crida A., Masset F., Nelson R. P., 2008, A&A, 478, 929
Paardekooper S.-J., Mellema G., 2006, A&A, 459, L17
Paardekooper S.-J., Mellema G., 2008, A&A, 478, 245
Paardekooper S.-J., Baruteau C., Crida A., Kley W., 2010, MNRAS, 401, 1950
Paardekooper S.-J., Baruteau C., Kley W., 2011, MNRAS, 410, 293
Stone J. M., Norman M. L., 1992, ApJS, 80, 753
Tanaka H., Takeuchi T., Ward W. R., 2002, ApJ, 565, 1257
Tassoul J. L., 1978, Theory of Rotating Stars. Princeton Univ. Press, Princeton, NJ

APPENDIX A: TEST CALCULATIONS WITH FARGOCA

The motion of the gas is described by the Navier–Stokes equations in a rotating frame in spherical coordinates as follows.

(i) Continuity equation:

$$\frac{\partial \rho}{\partial t} + \nabla \cdot (\rho \boldsymbol{v}) = 0, \tag{A1}$$

where ρ is the density of the gas and $\boldsymbol{v} = (v_r, v_\varphi, v_\theta)$ the velocity, with $v_\varphi = r \sin(\theta)(\omega + \Omega)$, where ω is the azimuthal angular velocity in the rotating frame.

(ii) Equations for the momenta. The Navier–Stokes equations for the radial momentum $J_r = \rho v_r$, the polar momentum $J_\theta = \rho v_\theta$ and the angular momentum $J_\varphi = \rho r \sin(\theta) v_\varphi = \rho r^2 \sin^2\theta(\omega + \Omega)$ read

$$\begin{cases} \frac{\partial J_r}{\partial t} + \nabla \cdot (J_r \boldsymbol{v}) = \rho[\frac{v_\theta^2}{r} + \frac{v_\varphi^2}{r} - \frac{\partial \Phi}{\partial r} \\ \qquad\qquad + \frac{1}{\rho}(f_r - \frac{\partial P}{\partial r})] \\ \frac{\partial J_\theta}{\partial t} + \nabla \cdot (J_\theta \boldsymbol{v}) = \rho r[\frac{v_\varphi^2 \cot(\theta)}{r} - \frac{1}{r}\frac{\partial \Phi}{\partial \theta} \\ \qquad\qquad + \frac{1}{\rho}(f_\theta - \frac{1}{r}\frac{\partial P}{\partial \theta})] \\ \frac{\partial J_\varphi}{\partial t} + \nabla \cdot (J_\varphi \boldsymbol{v}) = \rho r \sin(\theta)[-\frac{1}{r\sin\theta}\frac{\partial \Phi}{\partial \varphi} \\ \qquad\qquad + \frac{1}{\rho}(f_\varphi - \frac{1}{r\sin\theta}\frac{\partial P}{\partial \varphi})]. \end{cases} \tag{A2}$$

The function $f = (f_r, f_\varphi, f_\theta)$ is the divergence of the stress tensor (see, for example, Tassoul 1978). The potential Φ acting on the disc consists of the contribution of the star $\Phi_* = -GM_*/r$ and planets Φ_p, plus indirect terms that arise from the primary acceleration due to the planets and discs gravity.

To test the implementation of FARGOCA, we consider first the isothermal setup. The computational domain (r, φ, θ) consists of an annulus of the protoplanetary disc extending from r_{min} to r_{max}. In the vertical direction, the annulus extends from θ_D to $\pi - \theta_D$, the mid-plane being at $\theta = \pi/2$. We use a grid of $N_r \times N_\varphi \times N_\theta$ cells equally spaced in in r, φ, θ.

A1 Setup

We consider the gas at equilibrium in the gravitational field of the star, i.e. the motion is circular at constant height z. The vertical structure of the disc is provided by the hydrostatic equilibrium

in the thin-disc approximation. The initial density has a Gaussian profile

$$\rho(r, \theta) = f(r) \exp\left(- \frac{r^2(\frac{\pi}{2} - \theta)^2}{2H(r)^2} \right), \tag{A3}$$

where $H(r)$ is the height of the disc $H(r) = h_0 r^{1+\beta}$ with h_0 being the disc aspect ratio and β is the flaring index. The radial coordinate in the code is normalized by a_p. The function $f(r)$ is found setting the vertical integration of ρ equal to the disc surface density as

$$\Sigma(r) = \Sigma_0 r^{-\alpha_\Sigma} \tag{A4}$$

and reads

$$f(r) = \frac{\Sigma_0}{h_0 \sqrt{2\pi}} r^{-\alpha_\Sigma - 1 - \beta}. \tag{A5}$$

Let us remark that in the thin-disc approximation, we use $\cos(\theta) \simeq (\frac{\pi}{2} - \theta)$ and $r \sin(\theta) \simeq r$. The initial values of the velocities are $v_r = 0$ and $v_\theta = 0$, v_φ is obtained from the balance of the radial forces.

The initial conditions are obtained through an approximation so that they do not correspond exactly to the equilibrium, the gas is observed to relax towards a more stable state only marginally different from the initial configuration.

A2 FARGO algorithm in the 3D case

The specificity of the FARGO code (Fast Advection in Rotating Gaseous Objects; Masset 2000a) is a much larger timestep than usual hydrodynamical codes. The FARGO algorithm is particularly well suited to the description of a Keplerian disc where the traditional Courant condition provides very small timesteps due to the fast orbital motion at the inner boundary of the disc. In the FARGO algorithm, the timestep is limited by the perturbed velocity arising from the differential rotation. In order to extend this procedure to the 3D case, we consider the thin-disc approximation and we compute the mean velocity as

$$\bar{v}_\varphi(i) = \frac{1}{N_\varphi N_\theta} \sum_{j,h} v_\varphi(i, j, h), \tag{A6}$$

where the sum runs over the azimuthal and polar grid-cells. The local variation from the mean flow, i.e. the residual velocity, at each cell is then:

$$v_{i,j,h}^{res} = v_\varphi(i, j, h) - \bar{v}_\varphi(i),$$

which provides at each cell a limitation timestep

$$\delta t_\varphi = \frac{r \sin(\theta)\Delta\varphi}{v_{i,j,h}^{res}}. \tag{A7}$$

A normal CFL condition (Stone & Norman 1992) taking into account δt_φ provides the integration timestep.

A3 Parallelization

The use of a three-dimensional code for the study of gas–disc interaction with small-mass planets (less than 10 Earth masses) requires high-resolution grids. While in 2D, the parallel implementation of the code is in general not necessary, it becomes very important in the 3D case. For the specific nature of the FARGO algorithm, the Message Passing Interface (MPI) is implemented by splitting the mesh only radially in a number of rings equal to the number of MPI processes. The communications between neighbouring processors is done only
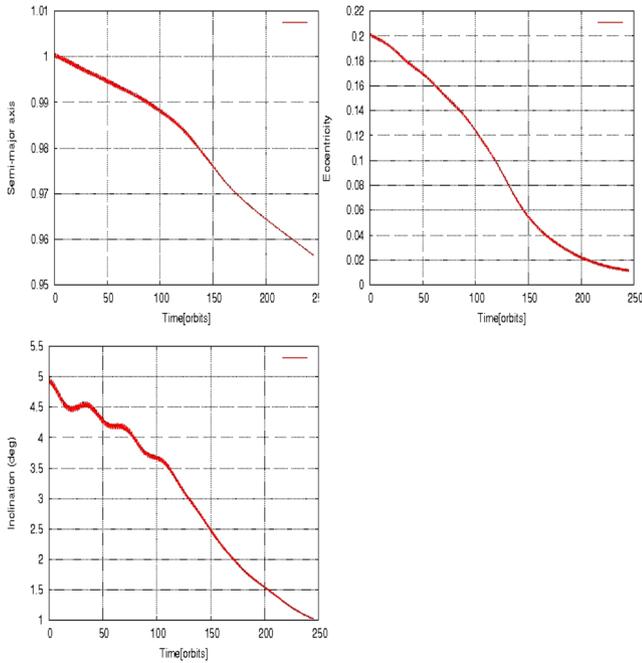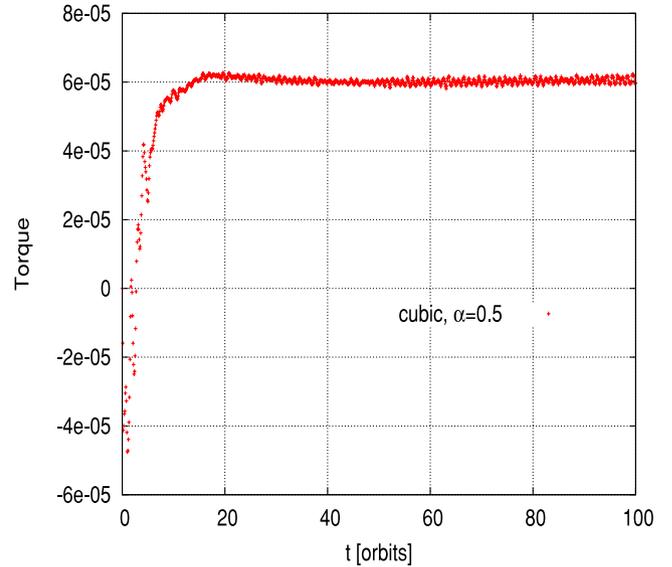
Figure A1. Evolution of the semi-major axis, eccentricity and inclination with time for a planet with initial inclination: $i_0 = 5°$ and initial eccentricity $e_0 = 0.2$.

Figure A2. Evolution of the total torque with time for a planet of $20\,M_{\oplus}$ in the radiative case for the cubic potential of equation (1) with $\alpha = 0.5$.

once per timestep in order to set the hydrodynamic variables in the ghost zones. The ghost zone is made of $5 \times N_s \times N_\theta$ grid-cells which is a relatively large number. Each MPI process has access to $N_r \times N_s \times N_\theta$ grid-cells with $N_r \geq 40$ being a good compromise between communication time and computation time. The N_r rings can then be further splitted on shared memory multicore processors using OpenMP instructions. We use in the following this hybrid parallelization which provided us an efficient code.

A4 Testing the isothermal configuration

In order to test the evolution of planet embedded in a 3D disc, we have repeated some of the experiments in Cresswell et al. (2007). The authors consider the evolution of a 20 Earth mass planet embedded in a 3D disc. They use, for the gravitational potential of the planet, the smoothed potential common in 2D simulations (equation 2) The planet is initially set at $a_{\rm p} = 5.2$ au ($r = 1$ in code units) in a disc of mass $M = 0.07 M_*$ extending from 2.08 to 13 au ($0.4 < r < 2.5$), with $\frac{H}{r} = 0.05$. The slope of the surface density is $\alpha_{\Sigma} = 0.5$ and the flaring index β is set to zero. The value of θ_D is $75°$ and the smoothing length is $r_{\rm sm} = 0.8 R_{\rm H}$. A Hill's cut is applied when estimating the torque of the disc on the planet. The resolution of the grid is $131 \times 388 \times 40$ ($N_r \times N_\varphi \times N_\theta$). For this kind of simulation, we use rigid boundaries in the radial and vertical directions; the problem is periodic in azimuth. In fig. 16 of Cresswell et al. (2007), the evolution of an orbit with initial inclination of $5°$ and initial eccentricity of 0.2 is studied. Fig. A1 shows the results obtained with FARGOCA which nicely agree with those of Cresswell et al. (2007).

A5 Testing the fully radiative disc

In order to test the fully radiative implementation, we have repeated some of the experiments presented in Kley et al. (2009) with the same disc setup. In the full radiative setup, the energy is initialized as follows:

$$E(r, \theta) = \frac{P(r, \theta)}{(\gamma - 1)} = \frac{h_0^2 \rho(r, \theta)}{(\gamma - 1)} r^{-1 - \alpha_\Sigma + 2\beta}. \tag{A8}$$

Contrary to the isothermal case, we have no analytical prescription for an initial radiative equilibrium state and we first obtain it numerically. The disc is axisymmetric in absence of the planet; therefore, we model it in 2D with coordinates (r, θ).

For the set of parameters chosen for this simulation, the balance between viscous heating and radiative cooling reduces the aspect ratio of the disc from the initial value of 0.05 to 0.037 as explained in Section 4.1. Once the 2D equilibrium is achieved, all the gas fields are expanded to 3D and a planet of $20\,M_{\oplus}$ is embedded in such an equilibrium disc and held on fixed circular orbits at $r = 1$, $\varphi = \pi$, $\theta = \pi/2$ (mid-plane). For this kind of simulation, we use reflecting boundaries in the radial and vertical directions; the problem is periodic in azimuth. Fig. A2 shows the evolution with time of the total torque acting on the planet (excluding of the inner part of the Hill sphere), for the cubic potential of equation (1) with $\alpha = 0.5$. The torque becomes almost constant after about 40 orbits, with a positive value of 6×10^{-5} in good agreement with the results of Kley et al. (2009, their fig. 14, top).

This paper has been typeset from a TEX/LATEX file prepared by the author.